Electronic Supplementary Information

Sub-4 nm $PtCu_3$ intermetallic catalyst with $L1_2$-ordered structure toward efficient activity and durability for oxygen reduction

Haibo Jiang,[a] Xiang Xie,[a] Liyuan Bi,[a] Shengwei Yu,[b] Jiaxi Zeng,[a] Lili Zhang,[a] Jianhua Shen[a] and Chunzhong Li*[b]*

a.) Shanghai Engineering Research Center of Hierarchical Nanomaterials, Key Laboratory for Ultrafine Materials of Ministry of Education, School of Materials Science and Engineering, East China University of Science & Technology; Shanghai 200237, China

b.) School of Chemical Engineering, East China University of Science and Technology, Shanghai 200237, China.

*.) Corresponding author.

E-mail address: jianhuashen@ecust.edu.cn; czli@ecust.edu.cn

Experimental section

Chemicals:

Chloroplatinic acid hexahydrate ($H_2PtCl_6 \cdot 6H_2O$, AR, 37.5wt%), Copper(II) chloride hexahydrate ($CuCl_2 \cdot 6H_2O$, AR,99wt%) and urea ($(NH_2)_2CO$, AR, 99.5wt%) were purchased from Aladdin. 20 wt% Pt/C was purchased from Shanghai Hesen Electric. Vulcan XC-72 was purchased from Macklin. All chemicals were used as received and not further purified.

Synthesis of $L1_2$-$PtCu_3$/C catalyst

In a typical synthesis,35 mg of urea, 30 mg of carbon black (Vulcan XC-72), 1.68 mL of $H_2PtCl_6 \cdot 6H_2O$ (10 mg/mL) with 25.6 mg of $CuCl_2 \cdot 2H_2O$ were sonicated for 1h to obtain a homogeneously dispersed black suspension. The suspension was flash frozen in liquid nitrogen and freeze dried overnight to obtain a dry solid black powder. The dried powder was then held in a tube furnace with the formation gas (5% hydrogen + 95% argon) at an elevated temperature rate of 10°C/min up to 550°C for 2h. To induce ordered transitions of the atoms at high temperatures, the furnace chamber was heated to 850 °C at a ramp rate of 5 °C/min for 2 h. After natural cooling to room temperature in the furnace chamber, the black solid powder was extracted, then washed several times with deionized water and heated at 60 °C for 8 hours in a vacuum oven to obtain $L1_2$-$PtCu_3$/C catalyst.

Synthesis of N-$PtCu_3$/C catalyst

The synthesis conditions were consistent with those of $L1_2$-$PtCu_3$ except that no urea was added to the precursor.

Materials characterization

The X-ray diffraction patterns of catalyst particles were collected on a D8 ADVANCE (Bruker, Germany) diffractometer in Cu K_α radiation (λ = 1.5406 Å) to determine the crystal structure and particle size. The operation voltage and current were

40 kV and 20 mA, respectively. The microstructure was analyzed using transmission electron microscopy (TEM) and high-resolution transmission electron microscopy (HRTEM) to analyze the micro-morphology operation by the JEOL-2100 experimental setup with LaB_6 cathode at 200 kV. High angle annular dark field scanning transmission electron (HAADF-STEM) imaging was performed on a Grand ARM 300F connected to an energy-dispersive X-ray spectroscopy (EDX). Inductively coupled plasma-atomic emission spectroscopy (ICP-AES) was manipulated to assess the concentration of the catalyst on Agilent 725ES. X-ray photoelectron spectroscopy (XPS) measurements were carried out using K-Alpha Plus (Somerfield, USA) with Al-Ka X-ray as the illuminant to Obtain the electronic structure and elemental composition of catalyst surfaces.

Electrochemical tests

All electrochemical measurements were operated in a standard three-electrode system. The glassy carbon electrode was mounted on a rotating disk electrode as the working electrode (5 mm in diameter), a saturated calomel electrode as the reference electrode, and a carbon rod as the counter electrode. Catalyst ink was obtained by dispersing 5 mg of catalyst powder in a mixture of 960 μL of isopropanol and 40 μL of Nafion (5 wt.%) and sonicated for 1 h. The catalyst film was obtained by depositing 4 μl of ultrasonically homogeneous catalyst ink on the glassy carbon electrode and drying naturally at room temperature. cyclic voltammetry curves were recorded in a 0.1 M $HClO_4$ aqueous solution passed through Ar at least 30 min with a potential interval of 0.06 V-1.3 V (vs RHE) and a scan rate of 100 mV s^{-1}. ORR polarization curves were recorded in 0.1 M $HClO_4$ solution saturated with O_2 using linear scanning voltammetry curves at 1600 rpm and a scan rate of 10 mV s^{-1}. Accelerated durability tests were performed in oxygen-saturated 0.1 M $HClO_4$ solution with a potential interval of 0.6-1.1 V (vs RHE) and a scan rate of 100 mV s^{-1}.

The ECSAs are determined from charges associated with underpotentially deposited H (H_{upd}).The electrochemical surface area of the catalyst is obtained from the following equation：

$$ECSA = \frac{Q_H}{C \times m_{Pt}} = \frac{S_H/v}{C \times m_{Pt}}$$

where Q_H is the charge consumed by the reaction (C m^{-2}), C is the charge value of hydrogen adsorbed on the Pt surface in the monolayer (210×10^{-2} μC cm^{-2}), S_H is the area of the H desorption area after subtracting the effect of the bilayer (V·mA), v is the scanning cycle rate (V s^{-1}) and m_{Pt} is the actual loading of Pt on the surface of the glassy carbon electrode (0.196 cm^{-2}). The integral area of the H desorption peak (Q_H) of the catalyst can be obtained from the cyclic voltammetry curve in the potential interval of 0.05 - 0.4 V vs. RHE.[1] The mass percentage of Pt in $L1_2$-$PtCu_3$ is measured by ICP-AES to be 16.85% with commercial Pt/C of 20.02%. Therefore, the actual loading (m_{Pt}) on the surface of the glassy carbon electrode is 3.37 μg and 4 μg, respectively.

The Koutecky-Levich equation was used to calculate the ORR kinetic currents:

$$\frac{1}{j_k} = \frac{1}{j_L} - \frac{1}{j} = \frac{1}{Bw^{1/2}} - \frac{1}{j}$$

where j_k, j_L, and j represent kinetic current density, limiting diffusion current density, and experimentally measured current density, respectively. B is a constant and w is the electrode rotation rate.

Density functional theory method

The first-principles density functional theory (DFT) calculations were performed in the Dmol3 code. Electron exchange and associated energies are described based on the generalized gradient approximation Perdew-Burke-Ernzerhof (GGA-PBE) generalization. Two numerical basis sets and the polarization function (DNP) are used to expand valence electrons, and the relativistic effect is simulated by DFT semi-core pseudopotential. Based on the image results of HAADF-STEM, the PtCu alloy covering two Pt atomic layers is modeled as the structure of $L1_2$-$PtCu_3$ with the pure Pt (111) as the reference. Simulations were carried out using a four-layer periodic cell, with the bottom two layers replacing the Cu atoms periodically with Pt atoms in the ratio Pt: Cu = 1:3, followed by cell structure optimization. The bottom two layers of

atoms are held in place, relaxing the rest. The Pt (100) surface was built to simulate $L1_2$-$PtCu_3$ with a two-layer Pt skin, and the vacuum layer was defined to be 10Å.

The oxygen reduction reaction involves the chemical adsorption of molecular O_2 on the catalyst surface and a four-electron transfer step of three oxygen-containing intermediates[2, 3]:

$$O_2 + * \rightarrow *O_2$$

$$*O_2 + H^+ + e^- \rightarrow *OOH$$

$$*OOH + H^+ + e^- \rightarrow H_2O + *O$$

$$*O + H^+ + e^- \rightarrow *OH$$

$$*OH + H^+ + e^- \rightarrow H_2O$$

* is considered to be an adsorption site on the catalyst surface.

The adsorption energy of the oxygen-containing intermediate was calculated by the following equation:

$$\triangle E(*OOH) = E(*OOH) - E(*) - [2E(H_2O) - 1.5E(H_2)]$$

$$\triangle E(*O) = E(*O) - E(*) - [2E(H_2O) - E(H_2)]$$

$$\triangle E(*OH) = E(*OH) - E(*) - [2E(H_2O) - 0.5E(H_2)]$$

The value of Gibbs free energy change for the oxygen-containing intermediate at a given potential is calculated by the following equation:

$$\triangle G(*OOH) = \triangle E(*OOH) + \triangle ZPE(*OOH) - \triangle TS(*OOH) - 3eU + 3\triangle G(ph)$$

$$\triangle G(*O) = \triangle E(*O) + \triangle ZPE(*O) - \triangle TS(*O) - 2eU + 2\triangle G(ph)$$

$$\triangle G4\ (*OH) = \triangle E(*OH) + \triangle ZPE(*OH) - \triangle TS(*OH) - eU + \triangle G(ph)$$

The value of Gibbs free energy change for each step at a given potential is calculated by the following equation:

$$\triangle G1 = \triangle G(*OOH) - 4(1.23 - eU)$$

$$\triangle G2 = \triangle G(*O) - \triangle G(*O)$$

$$\triangle G3 = \triangle G4\ (*OH) - \triangle G(*O)$$

$$\triangle G4 = -\triangle G4\ (*OH)$$

The Gibbs free energy value for each step at a given potential is calculated by the following equation:

$$G1 = 4.92$$

$$G2 = G1 + \triangle G1$$

$$G3 = G2 + \triangle G2$$

$$G4 = G3 + \triangle G3$$

$$G5 = G4 + \triangle G3$$

The oxygen adsorption energy i.e. E_{ads} (O) was calculated as:

$E_{ads}(O) = E_{total} - E(O) - E *$

E_{total}, E(O), and E* represent the energies of the oxygen adsorption system, O atoms, and without oxygen adsorption system, respectively.

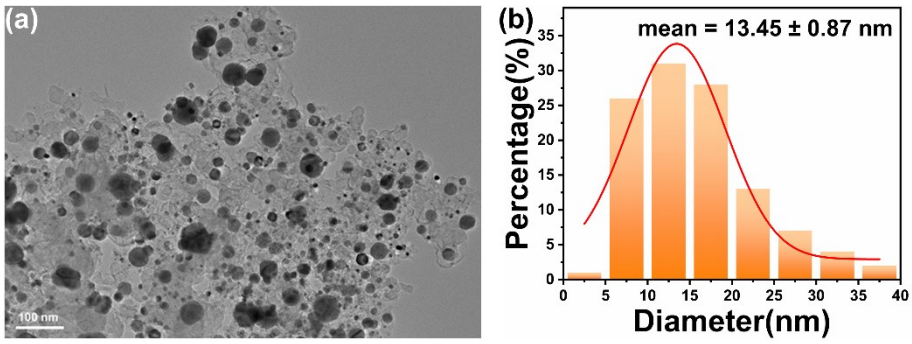

Fig. S1 (a) TEM images of annealed nanoparticles without urea protection. (b) The statistical distribution of the particle size.

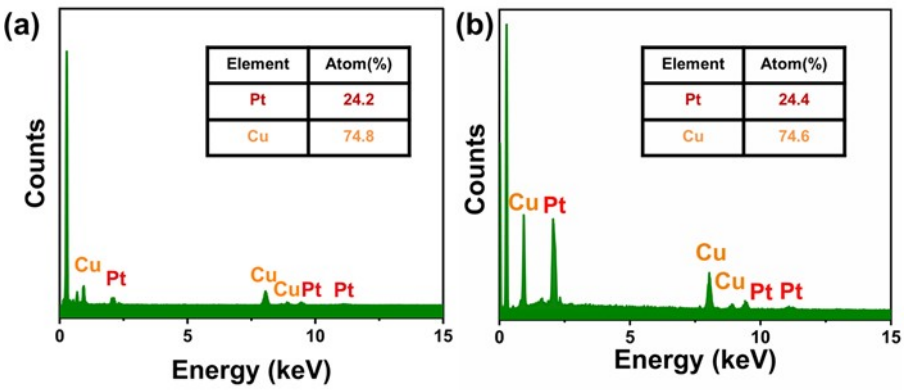

Fig. S2 EDS spectrum of $L1_2$-$PtCu_3$/C. Before (a) and after (b) electrochemical activation.

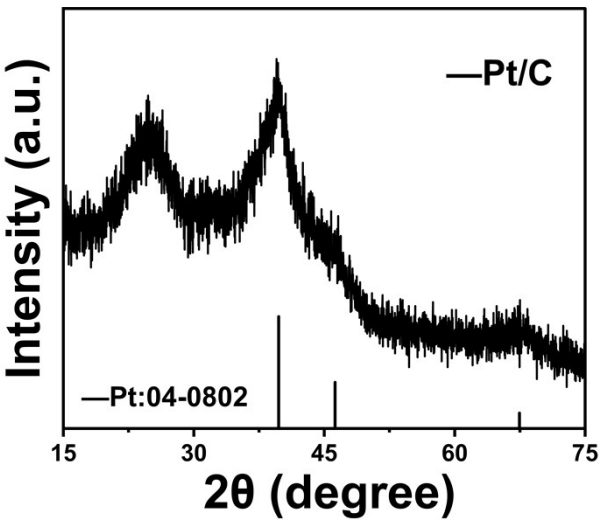

Fig. S3 XRD spectrum of Pt/C.

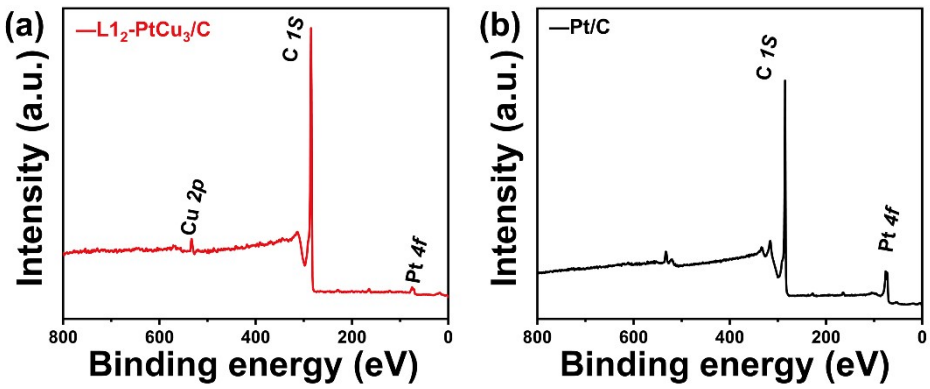

Fig. S4 XPS full survey spectra of L1$_2$-PtCu$_3$/C (a) and Pt/C (b).

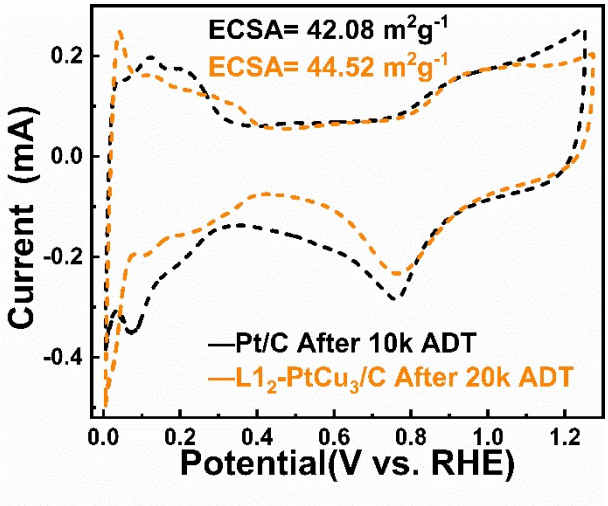

Fig. S5 Comparison of electrochemically active areas (ECSA) of $L1_2$-$PtCu_3$/C and Pt/C after different ADT cycles.

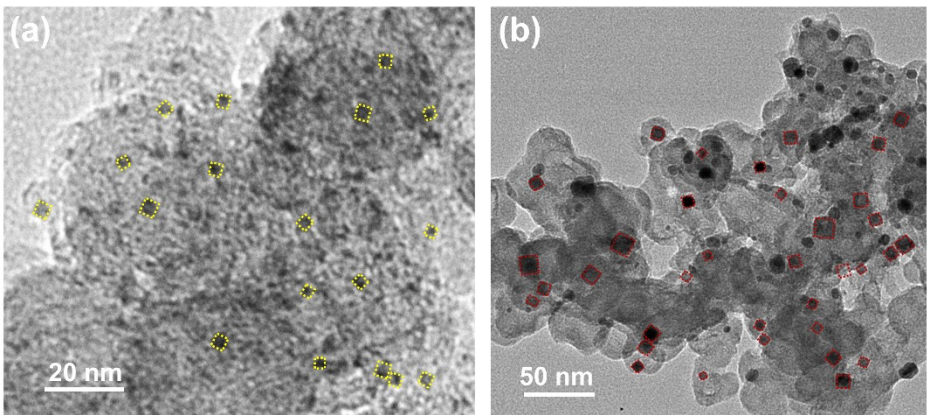

Fig. S6 TEM images of $L1_2$-$PtCu_3$/C before (a) and after (b) 20k ADT.

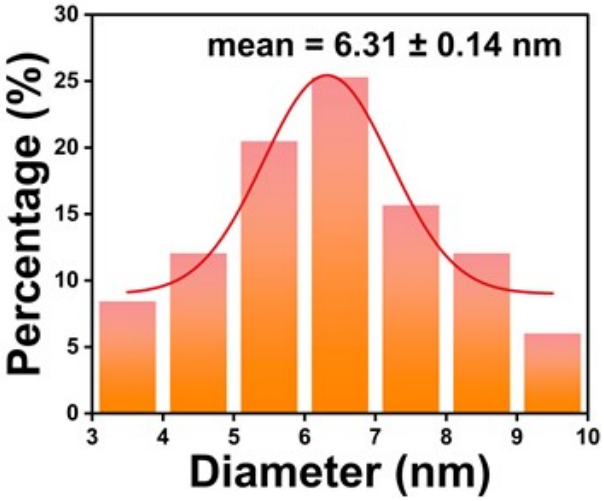

Fig. S7 Information on the particle size distribution of $L1_2$-$PtCu_3$/C after 20k ADT.

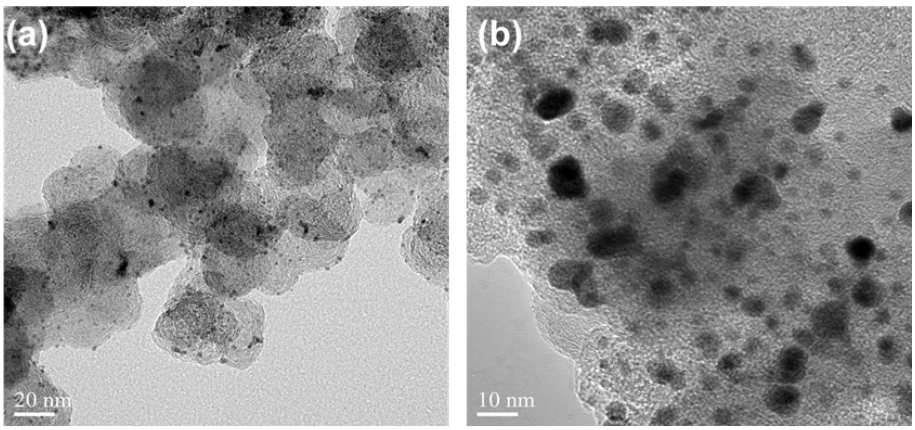

Fig. S8 TEM images of Pt/C before (a) and after (b) 10k ADT.

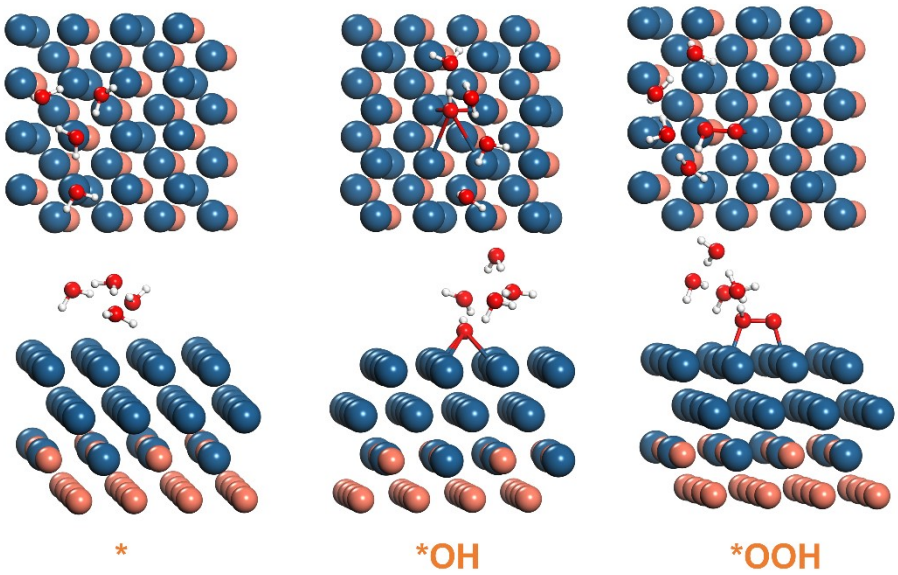

Fig. S9 Main (bottom) and top (top) views of the four electron reaction path atomic model of $L1_2$-$PtCu_3$, from left to right, is *, *OH and *OOH.

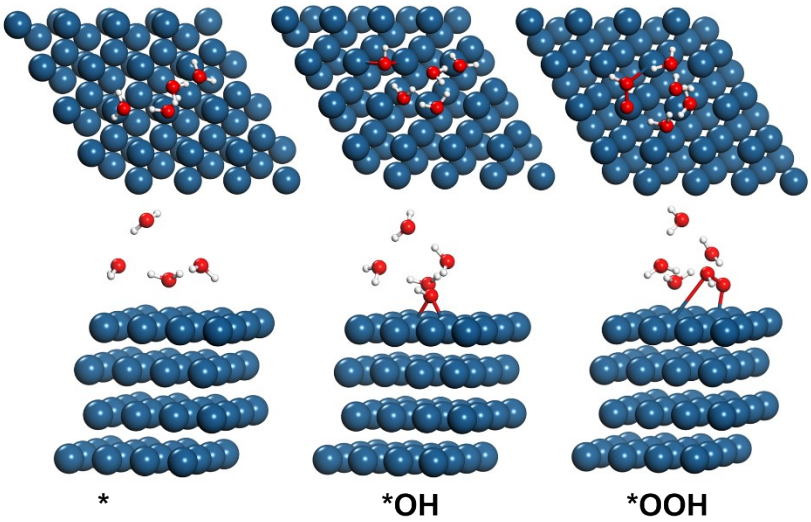

Fig. S10 Main (bottom) and top (top) views of the four electron reaction path atomic model of Pt (111), from left to right, is *, *OH and *OOH.

Table S1. Metal content of $L1_2$-$PtCu_3$/C measured using ICP-AES

	before 20k ADT		after 20k ADT	
Pt mass dispersion	17.43%		16.08%	
	wt%	at%	wt%	at%
Pt	49.44%	24.15%	50.82%	25.18%
Cu	50.56%	75.85%	49.18%	74.84%
Pt-Cu ratio	1:3.14		1:2.97	

The mass fraction of Pt before and after the 10k cycles for Pt/C are 20.02% and 17.78%.

Table S2. Rietveld refined fitting results of $L1_2$-$PtCu_3$/C and Pt/C

	XRD size (nm)	lattice constant	Lattice shrinkage (%)	lattice volume	R_{wp} (%)	GOF	Space group
$L1_2$-$PtCu_3$/C	6.42	3.70	-4.14	50.7	8.54	1.13	Pm-3m (221)
Pt/C	/	3.92	/	60.2	7.62	1.01	Fm-3m (225)

The lattice mismatch is calculated by the equation as follows:

$$\varepsilon = \frac{d_{L1_2-PtCu_3} - d_{Pt(bulk)}}{d_{Pt(bulk)}} = \frac{0.266 - 0.2775}{0.2755} = -4.14\%$$

Table S3. The Order Degree of XRD Refinement of $L1_2$-$PtCu_3$/C

	(100)/(111)	(100) order degree	(110)/(111)	(110) order degree
Standard Card	0.380	1	0.288	1
$L1_2$-$PtCu_3$/C	0.364	0.96	0.181	0.63

The order degree is calculated by the ratio of the peak heights between the ordered superlattice characteristic peaks and the main peaks to the corresponding peaks in the standard card.[4]

Table S4. Pt 4f peak splitting results for Pt/C and $PtCu_3$/C

		Pt/C	$PtCu_3$/C
Pt 4f	Pt $4f_{7/2}$	71.91 eV	71.20 eV
	Pt^{2+} $4f_{7/2}$	72.79 eV	71.75 eV
	Pt $4f_{5/2}$	75.42 eV	74.80 eV
	Pt^{2+} $4f_{5/2}$	76.91 eV	77.25 eV

Table S5. Comparison of intermetallic catalysts between particle size and ECSA

Catalyst	annealing temperature (°C)	TEM size (nm)	ECSA (m^2 g^{-1})	Reference
$L1_2$-$PtCu_3$/C	850	3.98	50.24	This work
Pt_1Co_1-IMC@Pt	700	5.30	43.50	[5]
fct-PtMn/C	800	4.30	28.90	[6]
Pt_1Fe_1-IMC/C	700	4.10	43.00	[4]
O-PtCuNF/C	300	28.80	35.10	[7]
Pt_3Mn intermetallic/C	700	4.23	44.00	[8]
$L1_0$-CoPt	700	5.00	/	[9]

Table S6. Comparison of RDE tests at 0.9 V vs. RHE based on intermetallic catalysts in this work and in orther studies.

Catalyst	Specific activity ($mA\ cm^{-2}$)	Mass activity ($A\ mg_{Pt}^{-1}$)	Reference
$L1_2$-$PtCu_3$/C	2.63	1.33	This work
Pt_1Co_1-IMC@Pt	1.1	0.53	[5]
fct-PtMn/C	1.43	0.41	[6]
Pt_1Fe_1-IMC/C	0.99	0.45	[4]
Pt_3Mn intermetallic/C	1.877	0.386	[8]
$L1_0$-CoPt	1.87	0.68	[9]
$PtCo_3$-H600	1.74	0.74	[10]
Pt_3Fe/C	1.364	0.454	[11]
$L1_0$-PtZn/C_{MOF}	1.13	0.926	[12]
Int-PtCuN/KB	1.18	1.15	[13]

Table S7. Electrochemical performance index depletion before and after accelerated durability testing of Pt/C and $L1_2$-$PtCu_3$/C. The specific activity and mass activity (MA) were calculated at 0.9V vs. RHE.

Catalyst		ECSA $m^2\ g_{Pt}^{-1}$	Specific activity $mA\ cm^{-2}$	Mass activity $A\ mg_{Pt}^{-1}$	MA loss after ADT
$L_{12}PtCu_3$/C	Intial	50.24	2.63	1.33	/
	20k cycles	44.52	2.18	0.97	27.1%
Pt/C	Intial	71.40	0.16	0.11	/
	10k cycles	42.08	0.15	0.063	42.7%

Table S8. Comparison of retention of MA between the present work and other electrocatalysts at different adt turn numbers.

Catalyst	Retention of MA (%)	Cycles (k)	Reference
$L1_2$-$PtCu_3$/C	72.2	20	This work
A-MS-$Pt_{1.5}$Ni	90.8	5	[14]
PtCo-1000/C	85.2	5	[15]
Pt_3Mn intermetallic/C	71.5	10	[8]
PtFe-H/Pt	77.0	10	[16]
PtZnCu-F-NC	70.0	10	[17]
Pt-Ni PNCs	64.1	10	[18]
$Pt_{2.4}$Ni/C	40.0	10	[19]
Pd-Se NPs/C	71.8	15	[20]
PtPd	74.4	15	[21]
PtCuNi-W/C	65.9	20	[22]
PtCo NFs	33.4	30	[23]
Ga-doped PtNi	39.1	30	[24]

Table S9. The Gibbs free energy value of $L1_2$-$PtCu_3$ and Pt (111)

	U vs. RHE (V)	G1 (eV)	G2 (eV)	G3 (eV)	G4 (eV)	G5 (eV)
$L1_2$-$PtCu_3$	U=0	4.92	3.44	2.07	0.95	0
	U=1.23	0	-0.22	-0.39	-0.28	0
Pt (111)	U=0	4.92	3.74	1.97	0.81	0
	U=1.23	0	0.046	-0.49	-0.42	0

Table S10. Lattice constants and lattice shrinkage of $L1_2$-$PtCu_3$ based on DFT calculations.

Catalyst	$a_{[100]}/a_{Pt}$	lattice contraction	$a_{[010]}/a_{Pt}$	lattice contraction	$a_{[001]}/a_{Pt}$	lattice contraction
$L1_2$-$PtCu_3$	0.942	5.72%	0.942	5.72%	0.942	5.72%

Reference

1. C. H. Yao, F. Li, X. Li and D. G. Xia, *J Mater Chem*, 2012, **22**, 16560-16565.
2. A. Kulkarni, S. Siahrostami, A. Patel and J. K. Norskov, *Chem Rev*, 2018, **118**, 2302-2312.
3. Z. Ma, Z. P. Cano, A. P. Yu, Z. W. Chen, G. P. Jiang, X. G. Fu, L. Yang, T. N. Wu, Z. Y. Bai and J. Lu, *Angew Chem Int Edit*, 2020, **59**, 18334-18348.
4. D. C. Lai, Q. Q. Cheng, Y. Zheng, H. Zhao, Y. B. Chen, W. B. Hu, Z. Q. Zou, K. Wen, L. L. Zou and H. Yang, *J Mater Chem A*, 2022, **10**, 16639-16645.
5. Q. Q. Cheng, S. Yang, C. H. Fu, L. L. Zou, Z. Q. Zou, Z. Jiang, J. L. Zhang and H. Yang, *Energ Environ Sci*, 2022, **15**, 278-286.
6. M. Song, F. Li, Q. Zhang, T. Shen, G. Luo, D. Li and D. Wang, *Chem Eng J*, 2023, DOI: 10.1016/j.cej.2023.147287.
7. H. Y. Kim, T. Kwon, Y. Ha, M. Jun, H. Baik, H. Y. Jeong, H. Kim, K. Lee and S. H. Joo, *Nano Lett*, 2020, **20**, 7413-7421.
8. J. Lim, C. Jung, D. Hong, J. Bak, J. Shin, M. Kim, D. Song, C. Lee, J. Lim, H. Lee, H. M. Lee and E. Cho, *J Mater Chem A*, 2022, **10**, 7399-7408.
9. J. Y. Guan, J. Q. Zhang, X. L. Wang, Z. P. Zhang and F. Wang, *Advanced Materials*, 2023, **35**.
10. Z. Wang, X. Yao, Y. Kang, L. Miao, D. Xia and L. Gan, *Advanced Functional Materials*, 2019, **29**.
11. C. Jung, C. Lee, K. Bang, J. Lim, H. Lee, H. J. Ryu, E. Cho and H. M. Lee, *Acs Appl Mater Inter*, 2017, **9**, 31806-31815.
12. T. Zhao, E. G. Luo, Y. Li, X. Wang, C. P. Liu, W. Xing and J. J. Ge, *Sci China Mater*, 2021, **64**, 1671-1678.
13. X. R. Zhao, H. Cheng, L. Song, L. L. Han, R. Zhang, G. H. Kwon, L. Ma, S. N. Ehrlich, A. I. Frenkel, J. Yang, K. Sasaki and H. L. Xin, *Acs Catal*, 2021, **11**, 184-192.
14. F. P. Kong, Z. H. Ren, M. N. Banis, L. Du, X. Zhou, G. Y. Chen, L. Zhang, J. J. Li, S. Z. Wang, M. S. Li, K. Doyle-Davis, Y. L. Ma, R. Y. Li, A. P. Young, L. J. Yang, M. Markiewicz, Y. J. Tong, G. P. Yin, C. Y. Du, J. Luo and X. L. Sun, *Acs Catal*, 2020, **10**, 4205-4214.
15. Y. F. Liao, L. S. Peng, C. L. Wu, Y. G. Yan, H. J. Xie, Y. G. Chen and Y. Wang, *Nano Res*, 2023, **16**, 10708-10709.
16. T. W. Song, M. X. Chen, P. Yin, L. Tong, M. Zuo, S. Q. Chu, P. Chen and H. W. Liang, *Small*, 2022, **18**.
17. T. Liu, F. Sun, M. H. Huang and L. H. Guan, *Acs Appl Energ Mater*, 2022, DOI: 10.1021/acsaem.2c01692.
18. T. Y. Xia, K. Zhao, Y. Q. Zhu, X. Y. Bai, H. Gao, Z. Y. Wang, Y. Gong, M. L. Feng, S. F. Li, Q. Zheng, S. G. Wang, R. M. Wang and H. Z. Guo, *Advanced Materials*, 2023, **35**.
19. G. D. Niu, M. Zhou, X. Yang, J. Park, N. Lu, J. G. Wang, M. J. Kim, L. D. Wang and Y. N. Xia, *Nano Lett*, 2016, **16**, 3850-3857.
20. Z. Y. Yu, S. L. Xu, Y. G. Feng, C. Y. Yang, Q. Yao, Q. Shao, Y. F. Li and X. Q. Huang, *Nano Lett*, 2021, **21**, 3805-3812.
21. R. F. Wu, P. Tsiakaras and P. K. Shen, *Appl Catal B-Environ*, 2019, **251**, 49-56.

22. W. Z. Tu, K. Chen, L. J. Zhu, H. C. Zai, E. Bin, X. X. Ke, C. F. Chen, M. L. Sui, Q. Chen and Y. J. Li, *Advanced Functional Materials*, 2019, **29**.
23. M. Wei, L. Huang, L. B. Li, F. Ai, J. Z. Su and J. K. Wang, *Acs Catal*, 2022, **12**, 6478-6485.
24. J. Lim, H. Shin, M. Kim, H. Lee, K.-S. Lee, Y. Kwon, D. Song, S. Oh, H. Kim and E. Cho, *Nano Lett*, 2018, **18**, 2450-2458.